The fracture flow equation and its perturbation solution

H. A. Basha and W. El-Asmar[1]

Faculty of Engineering and Architecture, American University of Beirut, Beirut, Lebanon

Received 10 July 2003; revised 18 September 2003; accepted 16 October 2003; published 20 December 2003.

[1] This work derives the fracture flow equation from the two-dimensional steady form of the Navier-Stokes equation. Asymptotic solutions are obtained whereby the perturbation parameter is the ratio of the mean width over the length of the fracture segment. The perturbation expansion can handle arbitrary variation of the fracture walls as long as the dominant velocity is in the longitudinal direction. The effect of the matrix-fracture interaction is also taken into account by allowing leakage through the fracture walls. The perturbation solution is used to obtain an estimate of the flow rate and the fracture transmissivity as well as the velocity and the pressure distribution in fractures of various geometries. The analysis covers eight different configurations of fracture geometry including linear and curvilinear variation as well as sinusoidal variation in the top and bottom walls with varying horizontal alignment and roughness wavelengths. The zero-order solution yields the Reynolds lubrication approximation, and the higher-order equations provide a correction term to the flow rate in terms of the roughness frequency and the Reynolds number. For sinusoidal and linear walls, the mathematical analysis shows that the zero-order flow rate could be expressed in terms of the maximum to minimum width ratio. For equal widths at both ends of the fracture, the first-order correction is zero. For sinusoidal fractures, the flow rate decreases with increasing Reynolds number and with increasing roughness amplitude and frequency. The effect of leakage is to create a nonuniform flow distribution in the fracture that deviates significantly from the flow rate estimate for impermeable walls. The derived flow expressions can provide a more reliable tool for flow and transport predictions in fractured domain. *INDEX TERMS:* 1832 Hydrology: Groundwater transport; 1829 Hydrology: Groundwater hydrology; 1831 Hydrology: Groundwater quality; *KEYWORDS:* fracture flow, Navier-Stokes equation, perturbation solution

Citation: Basha, H. A., and W. El-Asmar, The fracture flow equation and its perturbation solution, *Water Resour. Res.*, *39*(12), 1365, doi:10.1029/2003WR002472, 2003.

1. Introduction

[2] Fracture flow is commonly described by a simple equation relating the flux rate with the cube of the aperture width. This equation is known as the cubic law and originally describes the steady and laminar flow of a Newtonian fluid running between two smooth parallel plates. Such dynamic conditions and geometric uniformity simplify significantly the mathematical representation of the flow. However, recent experimental evidence and field studies have indicated that the validity of the cubic law is questionable [e.g., *Pyrak-Nolte et al.*, 1987; *Raven et al.*, 1988]. The cubic law exhibits the tendency to overestimate real flow rates; the measured transmissivity is lower than the predicted value and the velocity distribution within the fracture is not parabolic but rather skewed [*Brown et al.*, 1995; *Waite et al.*, 1998]. Attempts to explain the deviation of the experimental results from the theoretical predictions focused on studying the effect of nonuniform apertures, the roughness, and the tortuosity of the walls on the flow. In the absence of alternative procedures, corrections and improvements to the parallel plate model were made. Empirical and semiempirical models were developed in attempt to correct for those deviations. These include the inclusion of a correction factor [*Witherspoon et al.*, 1980], the extension to a two-dimensional aperture system using the Reynolds equation [*Brown*, 1987], the development of a conceptual channel model [*Tsang and Tsang*, 1987], and the incorporation of the effect of surface roughness and tortuosity in the Reynolds' equation [*Ge*, 1997]. Most of these improvements are based on the underlying cubic law assumptions, namely, that the flow behaves locally as in plane Poiseuille flow with a parabolic velocity profile, that the flux component perpendicular to the fracture plane is nonexistent, and that inertia effects are negligible.

[3] From a mathematical point of view, the high complexity of the flow conditions inside the fractures constituted a major obstacle to the development of a rigorous analysis. The description of flow in fractures should be based on the three-dimensional Navier-Stokes equation. For a one-dimensional steady parallel flow, the Navier-Stokes equation yields the cubic law equation. A natural extension is to include the two-dimensional (2-D) features of fracture flow using the two-dimensional version of the Navier-Stokes

[1]Now at the Department of Naval Architecture and Marine Engineering, University of Michigan, Ann Arbor, Michigan, USA.

0043-1397/03/2003WR002472

equations. Attempts to solve the 2-D Navier-Stokes equation analytically are relatively few. *Hasegawa and Izuchi* [1983] derived the perturbation solution of the two-dimensional equation for a related problem of flow through a channel bounded by one flat wall and one sinusoidal wall. *Kitanidis and Dykaar* [1997] presented a fourth-order perturbation solution by assuming that the Reynolds number is negligibly small so that the acceleration terms can be discarded. *Sisavath et al.* [2003] used the perturbation result of *Van Dyke* [1987] and the creeping flow assumption to relate the mean pressure drop with the mean flow rate and allow the estimation of the conductance or transmissivity of a fracture. The above analyses were restricted to either a symmetrical sinusoidal variation of both walls [*Kitanidis and Dykaar*, 1997; *Sisavath et al.*, 2003] or to a sinusoidal top wall with a flat bottom wall [*Hasegawa and Izuchi*, 1983].

[4] The previous studies assumed impermeable fracture walls. Such an assumption allowed the transformation of the governing equation and the elimination of the pressure terms using the definition of stream function. The stream function formulation reduces the number of dependent variables from three to one. However, it is restricted to flows between impermeable walls in which the side-leakage effects are neglected. The analysis of leakage necessitates the use of the Navier-Stokes equation expressed in its primary variables of velocity and pressure in order to apply the appropriate boundary conditions on the permeable walls. Furthermore, since the stream function formulations cancel the pressure terms and thereby bypass the need of pressure boundary conditions, a flow rate is normally defined at the boundary and the ensuing pressure drop across the fracture length is derived in order to obtain the expression for the transmissivity. However, in experimental setups, the pressure value at the entrance and at the exit of the fracture is prescribed and the flow rate is unknown. Hence pressure boundary conditions are more suitable for modeling and inverse analysis.

[5] The use of the cubic law is prevalent in solute transport models and other groundwater models that deal with fracture flow. A better description of fracture flow is therefore needed to provide a more reliable tool for flow and transport predictions in fractured domain. An approximate fracture flow equation can constitute a basis for the formulation of conceptual models for numerical modeling of flow in discrete fracture networks and in fractured soils wherein there is a significant interaction between the fracture and the enclosing soil matrix. In the present work, a theoretical study of fracture flow is presented in the hope of providing an adequate and simple equation for fracture flow estimation. Perturbation expansion of the two-dimensional Navier-Stokes equation is carried out to the second order whereby the perturbation parameter is the ratio of the mean width over the length of the fracture segment. An expansion to the fourth order is also presented for the case of Stokes flow within impermeable fracture walls. The second-order perturbation expansion takes into account the effect of inertia and the vertical viscous force component and can handle arbitrary variation of the top and bottom walls, whether symmetric or asymmetric. The effect of matrix-fracture interaction is also taken into account by allowing leakage into the soil matrix through the bottom fracture wall. The solution for leaky walls is more complicated than the impermeable wall case because the flow rate is not constant but varying with space.

[6] The present perturbation analysis assumes primarily that the mean fracture width is smaller than the fracture length and that the dominant velocity is in the longitudinal direction. The focus of the investigation is therefore directed toward the effect of the geometry of the fracture walls, the contribution of the neglected terms in the governing equation, and the effect of the leakage through the fracture planes rather than on the geometrical complexity of the flow paths. The perturbation solution is used to obtain the velocity and the pressure distribution in saturated fractures of various geometries from which flow rate expressions as well as expressions of the fracture transmissivity and of the friction factor are derived. The derived analytical results allow also the investigation of the various conditions under which the Reynolds and the Stokes approximations apply. Various wall configurations were examined, including linear and curvilinear variation as well as sinusoidal variation in the top and bottom walls with varying horizontal alignment and roughness frequency. The sinusoidal wall profile includes those of previous analytical and experimental works in which the top and bottom sinusoidal walls are aligned, misaligned, or symmetric about the center axis. In case of leaky fractures it is assumed that the seepage is through a flat bottom wall while the upper varying wall is impermeable.

[7] Section 2 derives the governing Navier-Stokes equations in dimensionless form, and section 3 uses perturbation expansion techniques to obtain an approximate second-order solution of the fracture flow equation and a fourth-order solution for the Stokes equation. Section 4 presents the flow rate expressions for the various geometries and flow conditions. Section 5 provides a discussion of the results, and section 6 concludes the study.

2. Theory

2.1. Governing Equations

[8] The governing equations of steady incompressible flow in saturated fractures are given by the Navier-Stokes equations in two-dimensional form

$$\frac{\partial u}{\partial x}+\frac{\partial w}{\partial z}=0 \tag{1}$$

$$u\frac{\partial u}{\partial x}+w\frac{\partial u}{\partial z}=-g\frac{\partial h}{\partial x}+\nu\left(\frac{\partial^2 u}{\partial x^2}+\frac{\partial^2 u}{\partial z^2}\right) \tag{2}$$

$$u\frac{\partial w}{\partial x}+w\frac{\partial w}{\partial z}=-g\frac{\partial h}{\partial z}+\nu\left(\frac{\partial^2 w}{\partial x^2}+\frac{\partial^2 w}{\partial z^2}\right) \tag{3}$$

Equation (1) is the continuity equation while the momentum equations are expressed by equations (2) and (3), where u and w are the velocity components in the x and z directions, respectively, ν is the constant kinematic viscosity, g is the gravitational acceleration and h is the piezometric head,

$h = p/\gamma + \zeta$, whereby p is the pressure, γ is the specific weight of water, and ζ is the coordinate pointing in the direction of g. The first two terms on the left-hand side of the momentum equations are the advective acceleration and represent the inertia effects; the third term is the head gradient while the last two terms represent the viscous forces. The dominant flow direction is denoted herein by the x-axis, while the direction perpendicular to the fracture plane is denoted by the z-axis.

2.2. Boundary Conditions

[9] The boundary conditions are given by the no-slip and seepage flux conditions on the fracture walls

$$\begin{aligned} z = b_t \quad u = 0 \quad w = 0 \\ z = b_b \quad u = 0 \quad w = q_b \end{aligned} \tag{4}$$

where b_t is the top width profile, b_b is the bottom width profile, and q_b is the seepage flux through the bottom wall into the adjoining matrix. The above conditions set that the upper wall is impermeable and that the leakage is only through the lower wall. For impermeable walls, the fracture has an arbitrary width distribution $b_t - b_b$, while for the leaky fracture case the leaky bottom wall is assumed to be flat. The general case of arbitrary bottom wall variation with leakage can be handled by the present perturbation approach, but the mathematics become too complicated and cumbersome with no additional gain in insight.

[10] The leakage flux q_b can be expressed using Darcy's law

$$q_b = k\frac{h_b - h}{d} \tag{5}$$

where $h = h(x, b_b)$ is the head at the bottom wall of the fracture and h_b is the hydraulic head at a distance d across the bottom matrix of a hydraulic conductivity k. It is herein assumed that steady state flow prevails in the fracture-matrix domain so that h_b is constant in time but varying in space.

[11] Additional boundary conditions are given by the prescribed uniform head conditions at the entrance and exit of the fracture

$$\begin{aligned} x = 0 \quad h = h_l \\ x = l \quad h = h_r \end{aligned} \tag{6}$$

Equation (6) implies that the pressure drop across the fracture length is known, from which an expression of the flow rate can be derived. Alternate boundary conditions to equation (6) were presented by previous investigators of the Navier-Stokes equation. The most common boundary condition is the specification of a constant flow [*Ge*, 1997; *Sisavath et al.*, 2003]. The classical Jeffrey-Hamel problem for a converging or diverging smooth walls assumes a particular form of the velocity distribution at the boundary [*Schlichting and Gersten*, 2000], which implies a nonuniform head distribution at the entrance and exit of the fracture [*Oron and Berkowitz*, 1998]. *Hasegawa and Izuchi* [1983] used an average formulation of the pressure gradient to relate the flow rate with the pressure drop, while *Kitanidis and Dykaar* [1997] formulated the auxiliary condition by equating the viscous dissipation with the work done by pressure forces using the energy equation.

2.3. Dimensionless Form

[12] Introducing the following dimensionless variables,

$$X = \frac{x}{l} \quad Z = \frac{z}{b_m} \quad U = \frac{ub_m}{q_o} \quad W = \frac{wl}{q_o} \quad H = \frac{h - h_r}{h_l - h_r} \quad R_e = \frac{q_o}{\nu} \quad \delta = \frac{b_m}{l} \tag{7}$$

where l is the length of the fracture, b_m is the mean aperture width, δ is a geometrical parameter representing the ratio of the mean aperture over the length of the fracture, and q_o is the cubic law flow rate per unit width of flow for a uniform fracture of mean width b_m [L^2/T],

$$q_o = \frac{b_m^3}{12}\frac{g}{\nu}\frac{\Delta h}{l} \qquad \Delta h = h_l - h_r \tag{8}$$

one obtains the following dimensionless form of the Navier-Stokes equations:

$$\frac{\partial U}{\partial X} + \frac{\partial W}{\partial Z} = 0 \tag{9}$$

$$\delta R_e\left(U\frac{\partial U}{\partial X} + W\frac{\partial U}{\partial Z}\right) = -12\frac{\partial H}{\partial X} + \delta^2\frac{\partial^2 U}{\partial X^2} + \frac{\partial^2 U}{\partial Z^2} \tag{10}$$

$$\delta^3 R_e\left(U\frac{\partial W}{\partial X} + W\frac{\partial W}{\partial Z}\right) = -12\frac{\partial H}{\partial Z} + \delta^4\frac{\partial^2 W}{\partial X^2} + \delta^2\frac{\partial^2 W}{\partial Z^2} \tag{11}$$

The dimensionless boundary conditions become

$$\begin{aligned} Z = B_t \quad U = 0 \quad W = 0 \\ Z = B_b \quad U = 0 \quad W = Q_b \end{aligned} \tag{12}$$

$$\begin{aligned} X = 0 \qquad H = 1 \\ X = 1 \qquad H = 0 \end{aligned} \tag{13}$$

where $B = b/b_m$. The dimensionless seepage term Q_b is obtained from equation (5) and the definition of W and H:

$$Q_b = \frac{q_b l}{q_o} = \lambda(H_b - H) \qquad \lambda = \frac{l}{q_o}\frac{k\Delta h}{d} \tag{14}$$

The parameter λ is the ratio of the flow into the matrix over the flow in the fracture. Hence it ranges from 0 for impermeable walls to near 1 for the improbable case of total seepage of fracture flow into the matrix.

[13] The above dimensionless variables are defined such that the continuity equation is satisfied at every order and that the head gradients in the X and Z directions are of the same order of magnitude. It should be noted that the above definition of the dimensionless velocities assumes that the ratio w/u is of the order δ, which implies that the dominant velocity is assumed to be in the longitudinal direction. Hence the present mathematical analysis cannot apply to flow in fractures in which the flow path is bidirectional. Note also that the definition of the dimensionless velocity variables is in terms of the parallel wall flux q_o as given by the cubic law (8). Hence the dimensionless flow rate is defined by $Q = q/q_o$ and numerical values of Q different

from 1 quantify the magnitude of the error in applying the cubic law.

3. Perturbation Solution

[14] Exact solutions to the Navier-Stokes equation are difficult to obtain except for the simplest flow cases in which the flow is one-directional. The prime example is the Couette-Poiseuille flow between parallel plates, whereby the nonlinear inertia terms vanish in a natural way, and Jeffery-Hamel flows between straight nonparallel walls, wherein the circumferential component of the velocity is equal to zero [*Schlichting and Gersten*, 2000]. However, one method to attain approximate solutions is through perturbation techniques that consist of expanding the nonlinear terms in a perturbation series to yield a set of linear differential equations. The choice of the perturbation parameter is instrumental in the success of the perturbation analysis. In the above equations, the choice of dimensionless variables produced the parameter δ.

[15] Defining the following perturbation series

$$U = U_0 + \delta U_1 + \delta^2 U_2 + \delta^3 U_3 + \delta^4 U_4 + O(\delta^5) \tag{15}$$

$$W = W_0 + \delta W_1 + \delta^2 W_2 + \delta^3 W_3 + \delta^4 W_4 + O(\delta^5) \tag{16}$$

$$H = H_0 + \delta H_1 + \delta^2 H_2 + \delta^3 H_3 + \delta^4 H_4 + O(\delta^5) \tag{17}$$

and substituting equations (15)–(17) into (9)–(11) and into (12)–(14), one obtains the differential equations and the associated boundary conditions at various orders. Fortunately, the perturbation expansion results in a series of ordinary differential equations that are amenable to an analytical solution.

3.1. Zero-Order Term

[16] The zero-order set of equations is

$$\frac{\partial U_0}{\partial X} + \frac{\partial W_0}{\partial Z} = 0 \tag{18}$$

$$\frac{\partial^2 U_0}{\partial Z^2} - 12\frac{\partial H_0}{\partial X} = 0 \tag{19}$$

$$-12\frac{\partial H_0}{\partial Z} = 0 \tag{20}$$

The zero-order boundary conditions are given by equations (12)–(13). Integrating the continuity equation (18) over the width of the fracture using the boundary conditions, one obtains

$$\frac{\partial Q_0}{\partial X} = Q_{b0} = \lambda(H_b - H_0) \tag{21}$$

where Q_{b0} is the zero-order dimensionless seepage rate. The zero-order steady flow rate Q_0 is obtained by integrating the zero-order velocity U_0 over the width. The velocity U_0 is the solution of equation (19) with the given boundary conditions. Equation (20) implies that the zero-order head H_0 is function of X only; hence the gradient $\partial H_0/\partial X$ in equation (19) is independent of Z and the integration of (19) is straightforward, yielding the parabolic velocity profile

$$U_0 = 6(Z - B_t)(Z - B_b)\frac{\partial H_0}{\partial X} \tag{22}$$

The flow rate Q_0 is then

$$Q_0 = \int_{B_b}^{B_t} U_0\, dZ = -B^3\frac{\partial H_0}{\partial X} \tag{23}$$

where $B(X) = B_t(X) - B_b(X)$. Substituting equation (23) into the continuity equation (21), one obtains the governing differential equation for the zero-order head distribution:

$$B^3\frac{\partial^2 H_0}{\partial X^2} + 3B^2B'\frac{\partial H_0}{\partial X} - \lambda H_0 + \lambda H_b = 0 \tag{24}$$

The term B' is the first derivative of B with respect to X. Using the boundary conditions, equation (24) can be solved to give the head distribution for any given simple width distribution B and matrix head distribution H_b. The flow rate is then derived from the head distribution H using equation (23).

[17] For impermeable wall surfaces, $Q_b = 0$, equation (21) yields that the flow rate Q_0 is constant. Integrating equation (23) over X, one gets the zero-order dimensionless head distribution. Substituting the boundary conditions and solving for Q_0, one obtains

$$Q_0 = \left(\int_0^1 \frac{dX}{B^3}\right)^{-1} \tag{25}$$

Equation (25) is the integrated cubic law equation that captures the primary characteristics of flow in fractures for impermeable fracture walls. It is also equivalent to the Reynolds approximation for one-dimensional flow.

3.2. First-Order Term

[18] The first-order equations are

$$\frac{\partial U_1}{\partial X} + \frac{\partial W_1}{\partial Z} = 0 \tag{26}$$

$$\frac{\partial^2 U_1}{\partial Z^2} - 12\frac{\partial H_1}{\partial X} = R_e\left(U_0\frac{\partial U_0}{\partial X} + W_0\frac{\partial U_0}{\partial Z}\right) \tag{27}$$

$$\frac{\partial H_1}{\partial Z} = 0 \tag{28}$$

with $W_1 = Q_{b1}$ at $Z = B_b$ and zero boundary conditions elsewhere. Integrating the continuity equation (26) over the width of the fracture, one obtains

$$\frac{\partial Q_1}{\partial X} = Q_{b1} = -\lambda H_1 \tag{29}$$

The right-hand side of equation (27) is function of the zero-order velocities and their gradients. The zero-order velocity W_0 is obtained from equations (18) and (22) using $W_0(B_b) = Q_{b0}$. Equation (28) implies also that H_1 is function of X only. Hence the first-order velocity U_1 can be obtained from

equation (27) by a straightforward integration over Z. Further integration over the width of the fracture yields the first-order flow rate

$$Q_1 = -B^3 H_1' + \frac{9}{70} R_e B' Q_0^2 - \frac{27}{140} R_e B Q_0 Q_0' \tag{30}$$

where $H' = \partial H/\partial X$ and $Q_0' = \partial Q_0/\partial X$. Substituting equation (30) into (29) yields the differential equation for the first-order head distribution

$$B^3 \frac{\partial^2 H_1}{\partial X^2} + 3B^2 B' \frac{\partial H_1}{\partial X} - \lambda H_1 = \frac{9R_e}{70} \frac{\partial}{\partial X}\left(B' Q_0^2 - \frac{3}{2} B Q_0 Q_0'\right) \tag{31}$$

The solution of equation (31) can be derived for a given width distribution and the zero boundary conditions on H_1. Having derived the first-order head distribution H_1, the first-order flow rate Q_1 is obtained from equation (30).

[19] For impermeable walls, the right-hand-side of equation (29) is zero, and consequently, the first-order flow rate is constant. Integrating equation (30) from $X = 0$ to $X = 1$ and using the zero boundary conditions on H_1, one obtains the first-order flow rate directly:

$$Q_1 = \frac{9R_e Q_0^3}{70} \int_0^1 \frac{\partial B}{\partial X} \frac{dX}{B^3} \tag{32}$$

One notices that for equal entrance and exit widths, $B(0) = B(1)$, the first-order term is zero since the integral in (32) cancels out. The first-order flow rate is also zero for Stokes flow $R_e = 0$.

3.3. Second-Order Term

[20] The second-order partial differential equations are

$$\frac{\partial U_2}{\partial X} + \frac{\partial W_2}{\partial Z} = 0 \tag{33}$$

$$\frac{\partial^2 U_2}{\partial Z^2} - 12\frac{\partial H_2}{\partial X} + \frac{\partial^2 U_0}{\partial X^2} = R_e\left(U_0 \frac{\partial U_1}{\partial X} + U_1 \frac{\partial U_0}{\partial X} + W_0 \frac{\partial U_1}{\partial Z} + W_1 \frac{\partial U_0}{\partial Z}\right) \tag{34}$$

$$12\frac{\partial H_2}{\partial Z} - \frac{\partial^2 W_0}{\partial Z^2} = 0 \tag{35}$$

The corresponding second-order boundary conditions are similar to the first-order boundary conditions. Integrating the second-order continuity equation (33) over the width of the fracture, one obtains

$$\frac{\partial Q_2}{\partial X} + \lambda H_{2b} = 0 \tag{36}$$

where $H_{2b} = H_2(X, B_b)$ is the head at the bottom wall. The second-order head distribution is not constant across the fracture width, unlike the lower-order head terms. The second-order flow rate Q_2 is derived from equation (34) using (35). Integrating (35), one gets

$$H_2(X, Z) = \frac{1}{12} \frac{\partial W_0}{\partial Z} + F(X) \tag{37}$$

Substituting equation (37) and the various zero- and first-order velocity expressions in equation (34) yields a second-order ordinary differential equation that can be integrated to obtain an expression of the second-order velocity U_2 in terms of $F'(X)$. Further integration of U_2 over the width yields the second-order flow rate Q_2 in terms of the lower-order flow rates and $F'(X)$

$$\begin{aligned} Q_2 = &- B^3 \frac{\partial F}{\partial X} + \frac{9}{35} R_e Q_0 Q_1 B' - \frac{27}{140} R_e Q_0 Q_1' B \\ &+ \frac{13 R_e^2 Q_0^3}{13475}\left[B'^2 - \frac{3}{4} B B''\right] \\ &+ \left[\left(\frac{3B_b}{B} + \frac{6B_b^2}{B^2} - \frac{3}{5}\right)B'^2 - \left(\frac{B}{10} + B_b + \frac{3B_b^2}{2B}\right)B''\right] Q_0 \\ &+ \left[\left(\frac{B}{2} + B_b\right)B_b'' - B_b'^2 - \left(4 + \frac{6B_b}{B}\right)B' B_b'\right] Q_0 \\ &- \left[\frac{27}{140} R_e Q_1 B + \left(\frac{B}{5} + 2B_b + \frac{3B_b^2}{B} + \frac{271}{92400} R_e^2 Q_0^2 B\right)B' \right. \\ &\left. - (B + 2B_b) B_b'\right] Q_0' - \frac{2929}{646800} R_e^2 Q_0 Q_0'^2 B^2 \\ &+ \left(\frac{B^2}{5} - \frac{R_e^2 Q_0^2 B^2}{8624} + \frac{B B_b}{2} + \frac{B_b^2}{2}\right) Q_0'' \end{aligned} \tag{38}$$

For leaky fracture walls, one must use equation (38) along with equation (36). Equation (38) is expressed in terms of the unknown function F. One must then relate the second-order head H_2 to the function F using (37) in order to use the remaining boundary conditions on H_2. Expressing the head H_b at the bottom wall $Z = B_b(X)$ in terms of F using (37), and substituting the resulting expression and equation (38) into the continuity equation (36), one obtains a second-order differential equation in F. The corresponding boundary conditions on F at $X = 0$ and at $X = 1$ are obtained by first integrating equation (37) over the width, substituting the boundary conditions on H_2, and expressing the resulting equation at $X = 0$ and at $X = 1$. Once the solution of the differential equation in F is obtained, one can then derive the expression for the second-order flow rate from equation (38).

[21] For impermeable walls, the flow rates at all orders are constant, as attested by equation (36). Equation (38) by itself can then be used to obtain the second-order flow rate. The function $F'(X)$ is first expressed in terms of the head H_2 by differentiating (37) over X and integrating the resulting expression over the width. Substituting the result in equation (38) and integrating from $X = 0$ to $X = 1$ using the boundary conditions on H_2, one obtains an expression for Q_2

$$\begin{aligned} \frac{Q_2}{Q_0} = &\frac{9 Q_0 Q_1 R_e}{35} \int_0^1 \frac{B'}{B^3} dX - Q_0 \\ &\int_0^1 \left[\frac{1}{10}\left(\frac{B'^2}{B^3} + \frac{B''}{B^2}\right) + \frac{B_b'}{B^3}\left(B' + B_b'\right)\right] dX + \frac{13 Q_0^3 R_e^2}{13475} \\ &\int_0^1 \left(\frac{B'^2}{B^3} - \frac{3B''}{4B^2}\right) dX \end{aligned} \tag{39}$$

3.4. Higher-Order Terms

[22] The number of terms grows exponentially as the order of the perturbation expansion increases. However, for

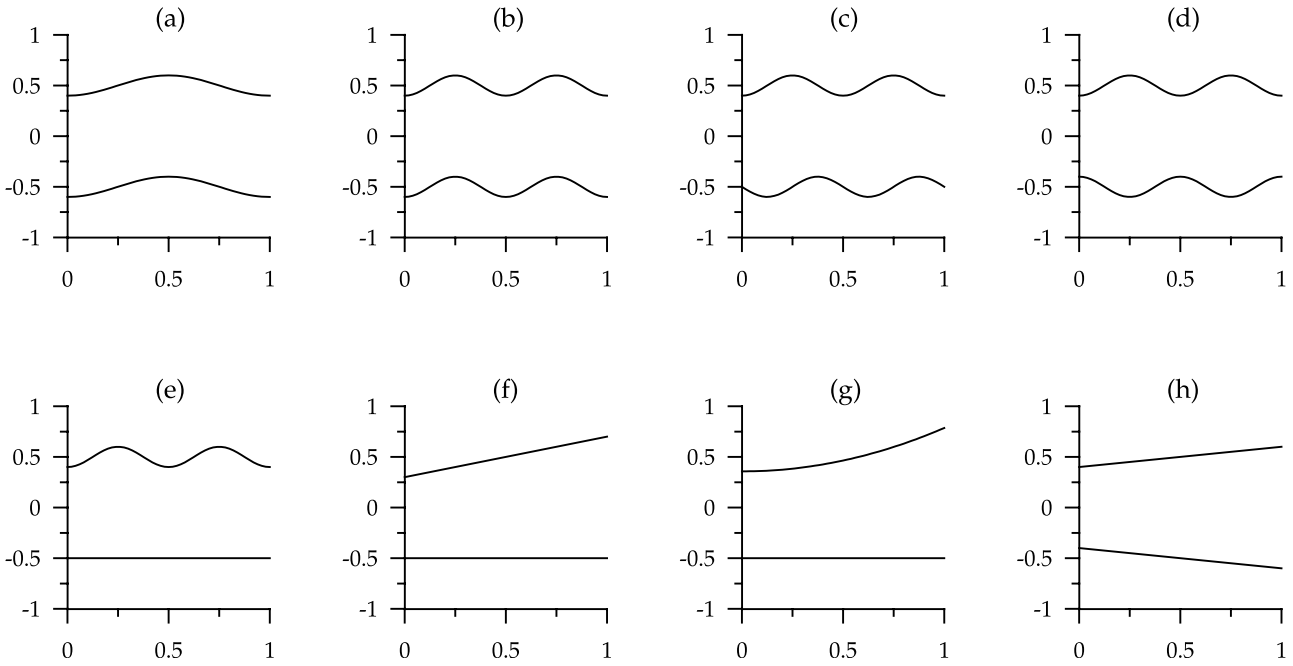

Figure 1. Fracture wall configurations: (a) one-cycle and (b) two-cycle mated sinusoidal walls ($\varepsilon = \pi$), two-cycle unmated sinusoidal walls with (c) $\varepsilon = 90°$ and (d) $\varepsilon = 0$, flat bottom wall with (e) sinusoidal top wall, (f) linearly and (g) quadratically varying top wall, and (h) linearly varying top and bottom walls (converging or diverging). The dimensionless amplitude of the sinusoidal variations is $a = 0.1$, and the maximum to minimum ratio is $\beta = 1.5$ for the other geometries.

creeping flow in which the Reynolds number is taken to be zero, the algebra can still be manipulated. The third-order term vanishes and the fourth-order term is the solution of the following set of equations:

$$\frac{\partial U_4}{\partial X} + \frac{\partial W_4}{\partial Z} = 0 \tag{40}$$

$$\frac{\partial^2 U_4}{\partial Z^2} + \frac{\partial^2 U_2}{\partial X^2} - 12\frac{\partial H_4}{\partial X} = 0 \tag{41}$$

$$\frac{\partial^2 W_2}{\partial Z^2} + \frac{\partial^2 W_0}{\partial X^2} - 12\frac{\partial H_4}{\partial Z} = 0 \tag{42}$$

For impermeable walls, the fourth-order flow rate is

$$\begin{aligned}\frac{Q_4}{Q_0} = &-Q_2\int_0^1 \frac{1}{10B^3}\left[\left(B'^2 + BB''\right) + 10B_b'\left(B' + B_b'\right)\right]dX + Q_0 \\ &\int_0^1 \frac{1}{5}\left[-\frac{23}{35}\frac{B'^4}{B^3} + \frac{188}{105}\frac{B'^2B''}{B^2} + \frac{1}{168}\frac{B''^2}{B} - \frac{17}{210}\frac{B'B'''}{B} - \frac{B^{iv}}{840}\right]dX \\ &+ Q_0\int_0^1 \frac{B_b'}{5B}\left[-2\frac{B'^3}{B^2} + \frac{1}{3}\frac{B'}{B}\left(14B'' + 10B_b''\right) - \frac{B'''}{6} - \frac{B_b'''}{3}\right]dX \\ &+ Q_0\int_0^1 \left[\frac{B_b'^2}{5B^3}\left(3BB'' - 2B'^2\right).\ + \frac{B_b''}{3B^2}\left(B'^2 - \frac{BB''}{20}\right) - \frac{1}{30B}\right. \\ &\left.\cdot\left(\frac{B_b''^2}{2} + B'B_b'''\right)\right]dX\end{aligned} \tag{43}$$

Equation (43) can be simplified further for a flat-bottom wall or for symmetrical walls.

4. Results

[23] In order to study the effect of wall geometry on fracture flow, various wall configurations were examined. Figure 1 presents the various fracture geometries in dimensionless coordinate systems. Although arbitrary variation of the walls can be handled by the perturbation solution, simplified geometries are more useful in shedding light on the fracture flow process. Three fracture configurations have a flat bottom wall and a varying top wall while the rest have both walls varying symmetrically and asymmetrically. The average dimensionless width is the same for all fractures and is equal to 1. The roughness wavelength is equal to one half of the fracture length in the two-cycle sinusoidal fractures (Figures 1b–1e), and it is equal to the fracture length in the other cases (Figures 1a and 1f–1h). The relative phase ε of the roughness elements for the top and bottom sinusoidal walls is varying from 0° to 180°. Figure 1b depicts mated sinusoidal walls with interlocking roughness ($\varepsilon = 180°$), Figure 1c show two out-of-phase sinusoidal walls ($\varepsilon = 90°$), while Figure 1d corresponds to unmated sinusoidal walls with mirror image roughness ($\varepsilon = 0°$). The sinusoidal wall profile includes those of previous analytical and experimental works in which the top and bottom sinusoidal walls are aligned or misaligned [*Brown et al.*, 1995] and symmetric about the center axis [*Kitanidis and Dykaar*, 1997; *Sisavath et al.*, 2003]. A parabolic shaped top wall (Figure 1g) is also included in order to compare with the linearly varying case (Figure 1f) and analyze the effect of the wall curvature on the flow. Figure 1h is an example of a

linearly diverging (or converging) symmetrical fracture. The fracture geometry in case of leaky walls was limited to parallel fracture walls and to linearly varying top wall (Figure 1f) in order to isolate the effect of matrix-fracture interaction on the flow from the effect of fracture geometry.

[24] The results presented herein are expressed in terms of the dimensionless flow rate Q. The second-order flow rate is expressed by $Q = Q_0 + \delta Q_1 + \delta^2 Q_2$ whereby the flow rate terms for impermeable walls are given by equations (25), (32), and (39). For Stokes flow $R_e = 0$ and impermeable walls, the flow rate to the fourth order is $Q = Q_0 + \delta^2 Q_2 + \delta^4 Q_4$ where Q_4 is given by equation (43). The flow rate terms for leaky walls are derived from the head distribution at various orders using equations (23), (30), and (38). The head distribution is obtained by solving the ordinary differential equations for the zero-order head (equation (24)), the first-order head term (equation (31)), and the second-order head term with their corresponding boundary conditions.

[25] The zero-order flow rate is the Reynolds approximation while the higher-order solution for $R_e = 0$ is the Stokes approximation. The higher-order solution for a nonzero R_e is the asymptotic solution of the full Navier-Stokes equations. The zero-order term accounts primarily for the geometry of the fracture while the higher-order terms account for inertia and other viscous effects. A value of Q different from 1 quantifies the magnitude of the error in applying the cubic law. The higher-order flow rate equations are also expressed as a ratio of the second-order flow rate over the zero-order flow rate. Hence a ratio Q/Q_0 different from 1 quantifies the deviation from the Reynolds approximation and indicates a significant contribution of inertia and the vertical viscous effect on the flow.

4.1. Impermeable Walls

4.1.1. Parallel Walls

[26] For a parallel wall fracture, $B(X) = 1$, and $B'(X) = B''(X) = 0$. The first- and second-order terms of the flow rate are then equal to zero. The second-order head distribution is linear, $H = 1 - X$, and the dimensionless flow rate reduces to 1 as expected.

4.1.2. Sinusoidal Variation

[27] For a sinusoidal fracture, the top width is given by

$$B_t(X) = \frac{1}{2} - a\cos(2n\pi X) \qquad 0 \le a \le \frac{1}{2} \tag{44}$$

while the bottom wall is either flat $B_b = -1/2$ or sinusoidal with varying longitudinal displacement:

$$B_b(X) = -\frac{1}{2} + a\cos(2n\pi X + \varepsilon) \qquad 0 \le \varepsilon \le \pi \tag{45}$$

The parameter a is the relative amplitude of the roughness element, n is another measure of roughness within the fracture, and ε is the relative phase of the roughness elements. Note that a is a dimensionless quantity normalized with respect to the mean width b_m. A value of $a = 0.25$ implies that the amplitude of the roughness is 25% of the mean width for a flat-bottom wall and 50% of the mean width for symmetrical walls with mirror image roughness. The maximum value of a for mirror walls is 0.5, at which there is a contact of the two walls. For $\varepsilon = \pi$, the sinusoidal fracture walls are aligned with no longitudinal displacement (Figure 1a–1b) while $\varepsilon = 0$ pertains to mirror walls (Figure 1d). Since the amplitude of the sinusoidal variation is smaller than the mean width, one can safely assume that the dominant flow is in the longitudinal direction.

4.1.2.1. Mated Walls Case

[28] The zero-order flow rate for mated sinusoidal walls ($\varepsilon = \pi$) is equal to the parallel wall flow rate $Q_{0s} = 1$. The first-order term for this case and the various sinusoidal configurations is equal to zero because for $B(0) = B(1)$ the integral in equation (32) cancels. However, the second-order flow rate (39) is different for each sinusoidal configuration because of the different contribution of the inertia and viscous effects. For $\varepsilon = \pi$, the fourth-order flow rate is

$$Q = 1 - 2a^2\pi^2 n^2\delta^2 + \frac{2}{5}a^2\left(1 + 10a^2\right)\pi^4 n^4\delta^4 \tag{46}$$

One notices that the contribution of the inertia term is zero for this case as the higher-order terms are independent of R_e.

4.1.2.2. Mirror Walls Case

[29] For symmetrical sinusoidal variations with mirror walls, the second-order flow rate is

$$\frac{Q}{Q_{0s}} = 1 - 2a^2 n^2\pi^2\,\frac{1 - 4a^2}{1 + 2a^2}\left(\frac{1}{5} + \frac{26R_e^2 Q_{0s}^2}{13475}\right)\delta^2 \tag{47}$$

where

$$Q_{0s} = \frac{\left(1 - 4a^2\right)^{5/2}}{1 + 2a^2} \tag{48}$$

4.1.2.3. Flat-Bottom Case

[30] For a flat-bottom sinusoidal fracture, the second-order approximation is given by

$$\frac{Q}{Q_{0s}} = 1 - a^2 n^2\pi^2\,\frac{1 - a^2}{2 + a^2}\left(\frac{6}{5} + \frac{26R_e^2 Q_{0s}^2}{13475}\right)\delta^2 \tag{49}$$

where

$$Q_{0s} = \frac{2\left(1 - a^2\right)^{5/2}}{2 + a^2} \tag{50}$$

Equation (49) agrees with equations (29) and (30) of *Hasegawa and Izuchi* [1983], which was also referenced by *Zimmerman and Yeo* [2000, equation (16)].

4.1.2.4. Misaligned Walls Case

[31] The second-order flow rate for an out-of-phase sinusoidal configuration with $\varepsilon = \pi/2$ is

$$\frac{Q}{Q_{0s}} = 1 - 2a^2 n^2\pi^2\left[\frac{3}{5}\,\frac{1 + 3a^2}{1 + a^2} + \frac{13Q_{0s}^2 R_e^2}{13475}\,\frac{1 - 2a^2}{1 + a^2}\right]\delta^2 \tag{51}$$

where

$$Q_{0s} = \frac{\left(1 - 2a^2\right)^{5/2}}{1 + a^2} \tag{52}$$

4.1.2.5. Zero-Order General Case

[32] The zero-order flow rates (48), (50), and (52) for the various alignments of the sinusoidal walls (Figures 1a–1e)

can be expressed by a single formula in terms of the minimum width $\gamma = b_{\min}$

$$Q_{0s} = \frac{2[\gamma(2-\gamma)]^{5/2}}{3-\gamma(2-\gamma)} \tag{53}$$

where $\gamma = 1$ for $\varepsilon = \pi$ (Figures 1a and 1b), $\gamma = 1 - \sqrt{2}a$ for $\varepsilon = \pi/2$ (Figure 1c), $\gamma = 1 - \sqrt{3}a$ for $\varepsilon = \pi/3$, $\gamma = 1 - \sqrt{2+\sqrt{2}}a$ for $\varepsilon = \pi/4$, $\gamma = 1 - 2a$ for $\varepsilon = 0$ (Figure 1d), and $\gamma = 1 - a$ for the flat-bottom wall (Figure 1e). Hence the zero-order flow rates for a sinusoidal fracture with a flat-bottom wall and for sinusoidal fracture walls with $\varepsilon = 120°$ are equal since the minimum width for both cases is $1 - a$. The zero-order flow rate can also be expressed in terms of $\beta = b_{\max}/b_{\min}$

$$Q_{0s} = \frac{64\beta^{5/2}}{(\beta+1)^3(3+2\beta+3\beta^2)} \tag{54}$$

A similar generalization to the second-order flow rate is not possible because the effects of viscous and inertia forces are different for the different sinusoidal configurations.

[33] The zero-order solutions show that the zero-order flow rate is independent of the roughness frequency n and of the misalignment of the roughness corrugations ε. The presence of the factor $n\delta$ implies that the higher-order solutions are dependent on the period of the wall waviness. The number of cycles n can increase as long as δ is small such that $n\delta$ is within limits. The terms n and δ always appear as a factor in all the higher-order terms, proving that the flow rate for the head drop in n cycles is equivalent to the flow rate for an average head drop per cycle. The product $an\delta$ can also be expressed in terms of the slope of the roughness since the product in dimensional terms is independent of the width and function of the amplitude to wavelength ratio $\bar{a}n/l$. Hence the various solutions can estimate the flow rate for a decreasing mean aperture, without a change in the roughness amplitude and wavelength, by increasing a while keeping $an\delta$ constant. The second-order solutions show that the deviation of the flow rate from its zero-order estimate is of the second-order δ^2, which partly explains the small contribution of the higher-order terms and the robustness of the Reynolds approximation for the sinusoidal configuration for small δ. Moreover, the second-order flow rates for the various sinusoidal alignments are dependent on a^2 as can be shown from Taylor's series expansion for small a. This shows that the discharge is affected slightly by the roughness amplitude if the corrugations do not approach the center (i.e., small a).

4.1.3. Linear and Curvilinear Variation

[34] For a linear variation in the fracture width, the top width is given by

$$B_t(X) = \frac{1}{c+1}\left(\frac{1}{2} + cX\right) \tag{55}$$

while the bottom wall is either flat $B_b = -1/2$ or linearly varying in a mirror image of the top width $B_b(X) = -B_t(X)$. The zero-order flow rate can be expressed in a single formula for the linearly varying wall whether converging or diverging (Figure 1g) or with a flat bottom (Figure 1f)

$$Q_{0l} = \frac{16m^2}{(m+1)^4} \tag{56}$$

The parameter $m = B(1)/B(0)$ is the ratio of the width at the exit over the width at the entrance. It can be considered as a measure of the extent of nonuniformity in the fracture width. Values of m greater than 1 imply a diverging fracture, while values of m less than 1 are for converging fracture walls. For diverging fractures, the definition of m is equivalent to the maximum to minimum width ratio β used in equation (54). The relationship between the slope c and the parameter m for the flat bottom wall is $c = 2(1-m)/(m-3)$, and for the symmetrical case, it is $c = (m-1)/2$. The opening half-angle α of the diverging or converging fracture can also be expressed in terms of m using the geometrical result $\tan\alpha = (m-1)/(m+1)$ for the symmetrical case and $\tan\alpha = 2(m-1)/(m+1)$ for the flat-bottom case.

4.1.3.1. Symmetrical Linear Profile

[35] For a symmetrical linear variation of both walls, the second-order flow rate is

$$\frac{Q_l}{Q_{0l}} = 1 + \frac{1}{35}\frac{m-1}{m+1}\left[9R_eQ_{0l} + \frac{m-1262R_e^2Q_{0l}^2+1155}{m+1}\frac{\delta}{55}\right]\delta \tag{57}$$

The flow rate in the linear wall configuration is function of the first-order δ and is nonzero, unlike the case for sinusoidal walls. Hence the effect of the roughness frequency is to the first-order, and its contribution is larger in the linear case than in the sinusoidal case where it was of order δ^2. For Stokes approximation, the fourth-order flow rate is

$$\frac{Q_l}{Q_{0l}} = 1 + \left(\frac{m-1}{m+1}\right)^2\left[\frac{3}{5} - \frac{1}{7}\left(\frac{m-1}{m+1}\right)^2\delta^2\right]\delta^2 \tag{58}$$

One notices that for Stokes flow, the fourth-order flow rate is the same whether the fracture is converging or diverging. It is the first-order term that takes into account the nature of the flow.

4.1.3.2. Asymmetrical Linear Profile

[36] The second-order flow rate for a flat-bottom wall and linearly varying top wall is

$$\frac{Q_l}{Q_{0l}} = 1 + \frac{1}{35}\frac{m-1}{m+1}\left[9R_eQ_{0l} + \frac{m-1262R_e^2Q_{0l}^2-770}{m+1}\frac{\delta}{55}\right]\delta \tag{59}$$

For symmetrical fractures and flat-bottom walls, the solution is similar in form except for the numerical coefficient that is the result of the vertical viscous dissipation. However, the terms proportional to R_e are the same in equations (57) and (59). The inertia effect terms always include the factor $R_eQ_o\delta$ where Q_0 is the Reynolds approximation. The definition of the Reynolds number R_e in equation (7) is expressed in terms of the flow rate for a parallel fracture, which is constant for all fractures with

equal mean width. Therefore the term $R_e^* = R_e Q_0$ accounts for the variation of geometry and the factor δR_e^* accounts for the spatial frequency of the fracture. The fourth-order Stokes flow rate is

$$\frac{Q_l}{Q_{0l}} = 1 - \frac{2}{5}\left(\frac{m-1}{m+1}\right)^2\left[1 + \frac{34}{7}\left(\frac{m-1}{m+1}\right)^2\delta^2\right]\delta^2 \qquad (60)$$

4.1.3.3. Parabolic Profile

[37] In order to study the effect of curvature on the flow, a parabolic variation is assumed for the top wall (Figure 1h) given by

$$B_t(X) = \frac{3}{2c+3}\left(\frac{1}{2} + cX^2\right) \qquad (61)$$

while the bottom wall is flat, $B_b = -1/2$. The zero-order flow rate is expressed by

$$Q_{0p} = \frac{216m^2\sqrt{m-1}}{(m+2)^3\left[\sqrt{m-1}(3m+2) + 3m^2\arctan\sqrt{m-1}\right]} \qquad (62)$$

where $m = B(1)/B(0)$ and is related to c by $c = 3(1-m)/(m-4)$. Other wall configurations can similarly be handled; however, a numerical evaluation of the integral terms might then be necessary.

4.2. Leaky Walls

4.2.1. Parallel Walls

[38] The solution of equation (24) for parallel walls ($B = 1$), and uniform H_b is

$$H_0(X) = \sinh\left[(X-1)\sqrt{\lambda}/2\right] \cdot \left[(1-2H_b)\frac{\sinh\left(X\sqrt{\lambda}/2\right)}{\cosh\left(\sqrt{\lambda}/2\right)} - \frac{\cosh\left(X\sqrt{\lambda}/2\right)}{\sinh\left(\sqrt{\lambda}/2\right)}\right] \qquad (63)$$

The zero-order flow rate is obtained from equation (23)

$$Q_0(X) = \frac{\sqrt{\lambda}}{\sinh\sqrt{\lambda}}\left[H_b\cosh\left(X\sqrt{\lambda}\right) + (1-H_b)\cosh\left[(X-1)\sqrt{\lambda}\right]\right] \qquad (64)$$

The first-order flow rate can be obtained by solving equation (31) and similarly for the second-order flow rate. The total seepage loss through the bottom fracture wall is then given by $Q(0) - Q(1)$.

4.2.2. Linear Variation

[39] For a linear variation in the top fracture wall with a head-dependent leakage through the bottom wall, the zero-order head distribution for $H_b = 0$ is given by equation (24) whereby the width B is expressed in terms of m. The solution is in terms of the modified Bessel functions of the first and second kind [*Hildebrand*, 1976, p. 153]

$$H_0(X) = \frac{1}{1+(m-1)X}\frac{I_2[A(1)]K_2[A(X)] - I_2[A(X)]K_2[A(1)]}{I_2[A(1)]K_2[A(0)] - I_2[A(0)]K_2[A(1)]} \qquad (65)$$

where $A(X) = \sqrt{\lambda/B}(m+1)/|m-1|$. The zero-order flow rate is obtained from equation (23).

5. Discussion

5.1. Conductance

[40] Various definitions exist for quantifying the hydraulic conductivity of a fracture. The dimensionless transmissivity $\overline{T}$ is defined by $Q = -\overline{T}dH/dX$. Since the dimensionless gradient is $dH/dX = -1$, the dimensionless transmissivity $\bar{T}$ becomes then equal to Q. The dimensional transmissivity is $T = b_m{}^3 g\overline{T}/\nu$.

[41] The permeability of a fracture is also quantified in terms of an equivalent hydraulic aperture B_e that would yield the same flow rate when substituted in the cubic law $Q = -B_e^3\partial H/\partial X$. Hence the dimensionless transmissivity and the equivalent hydraulic aperture are equal, i.e., $B_e{}^3 = \overline{T} = Q$. The dimensional hydraulic aperture is $b_e = b_m B_e$.

[42] Another relationship between the head drop and the mean velocity can be formulated using the definition of the friction factor f as $-dh/dx = (f/d_h)(V_m^2/2g)$ where $V_m = q/b_m$ is the mean velocity and $d_h = 2b_m$ is the hydraulic diameter [*Schlichting and Gersten*, 2000, p. 103]. Defining the Reynolds number in terms of the hydraulic diameter and the mean velocity, $R_e^h = V_m d_h/\nu$ and using equation (7) and $dH/dX = -1$, the friction factor relationship becomes $fR_e^h = 96/Q$, which shows that the friction factor is inversely related to the flow rate. For decreasing values of Q, the friction factor increases, while for $Q = 1$ it reduces to the friction factor relationship for laminar flow conditions. Note that $R_e^h = 2R_e^* = 2R_e Q_0$ if Q is given by the zero-order flow rate.

[43] In summary, the second-order flow rates Q presented in the previous section permit the estimation of the transmissivity, equivalent hydraulic aperture, and the friction factor for various geometries and flow conditions.

5.2. Effect of Geometry

[44] The zero order flow rate is the Reynolds approximation that captures the sole effect of the fracture geometry on the flow without the additional effect of roughness frequency and inertia. Figure 2 presents the zero-order flow rate for a sinusoidal fracture with varying longitudinal displacement of the bottom wall. Equations (48), (50), and (52) are used to plot the corresponding curves. For no displacement ($\varepsilon = \pi$), the zero-order flow rate is equal to the parallel wall flow rate, i.e., $Q_0 = 1$. For increasing longitudinal displacement, the flow rate decreases significantly. For $\varepsilon = \pi/2$, the zero-order flow rate decreases by 10% to $Q_0 = 0.9$ for $a = 0.125$ and by more than 30% to $Q_0 = 0.67$ for $a = 0.25$. For mirror sinusoidal walls ($\varepsilon = 0$), the zero-order flow rate decreases further to 0.43 for $a = 0.25$, which implies a 57% decrease from the cubic law prediction. By comparing the slope of the curves in Figure 2, one notices that Q decreases faster for larger values of a than for smaller values of a. This finding agrees with experimental observations in which the initial linear decrease of the effective permeability with a is followed by a more rapid decrease for increasing values of a.

[45] The above variations can be represented by a single curve using equation (53) or (54) as shown in Figure 3, which presents the zero-order flow rate as a function of β for a linear, parabolic, and a sinusoidal fracture. The parameter

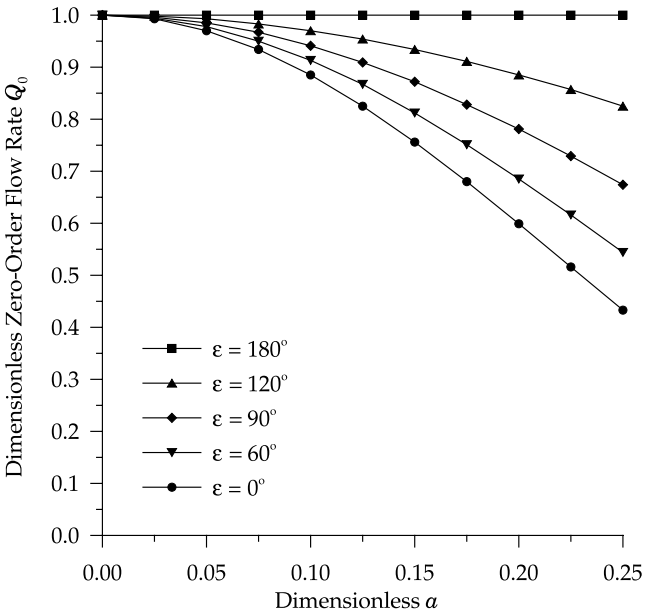

Figure 2. Zero-order flow rate for a sinusoidal fracture with various horizontal alignments ε of the bottom wall. The flow rate for a parallel wall fracture of equivalent mean width is equal to 1.

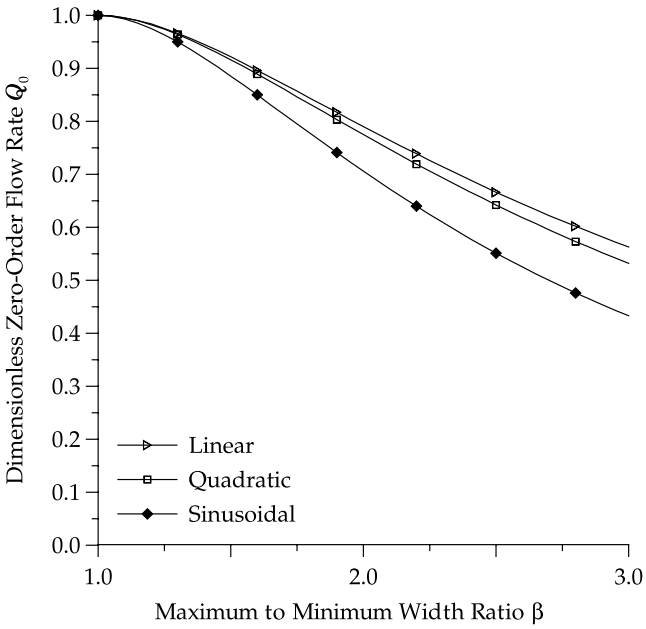

Figure 3. Zero-order flow rate for a linear, quadratic, and sinusoidal wall as a function of the maximum to minimum width ratio β.

$\beta = b_{max}/b_{min}$ is equivalent to m for a diverging fracture and to $1/m$ for a converging fracture. Equations (54), (56), and (62) are used to generate the three curves. For the parallel wall case $\beta = 1$, the second-order flow rate is equal to 1, as expected. Figure 3 shows that in terms of β, the zero-order flow rate variations are quite close. The parabolic variation produces a slight decrease over the linear wall case. For $\beta = 2$, the flow rate decreases by 20% to 30%, but the difference between the linear and the parabolic fracture is within 2% and it is roughly 10% between the sinusoidal fracture and the linear one. The decrease in the flow rate for a linear wall profile and increasing values of m as shown in Figure 3 agrees with Figure A3 by *Oron and Berkowitz* [1998] in which the discharge decreases with increasing value of α.

5.3. Effect of Roughness

[46] Figure 4 presents the second-order flow rate as a function of the amplitude of the sinusoidal corrugations for one-cycle ($n = 1$) and two-cycle ($n = 2$) roughness wavelengths with $\delta = 0.3$. Hence the roughness frequency is $n\delta = 0.3$ for $n = 1$ and $n\delta = 0.6$ for $n = 2$. The three sets of curves pertain to the case of aligned sinusoidal fractures (Figures 1a and 1b), mirror sinusoidal walls (Figure 1d), and sinusoidal fracture with a flat-bottom wall (Figure 1e). Equations (46), (47), and (49) are evaluated using $R_e = 0$ in order to isolate the effect of inertia from the viscous dissipation. Since the parameter n appears only in the second-order term, a large difference between the curves $n = 1$ and $n = 2$ indicates the importance of the second-order term and the significant contribution of the vertical viscous effects on the flow rate. For symmetrical walls ($\varepsilon = 0$), the effect of the increased roughness is relatively small since the curve for the one-cycle and the two-cycle are very close. On the other hand, the second-order flow rate for mated sinusoidal walls ($\varepsilon = \pi$) decreases significantly with increasing roughness cycles ($n = 2$), indicating the increasing effect of the vertical viscous dissipation. The strong dependence of Q on $n\delta$ for $\varepsilon = \pi$ shows the limitation of the zero-order equation in capturing the flow characteristic for this fracture geometry. The case of the fracture bounded by one flat wall and one sinusoidal wall shows a similar trend; however, the decrease in the second-order flow rate for $n = 2$ is smaller than the decrease for the other two cases in which both walls are varying, because

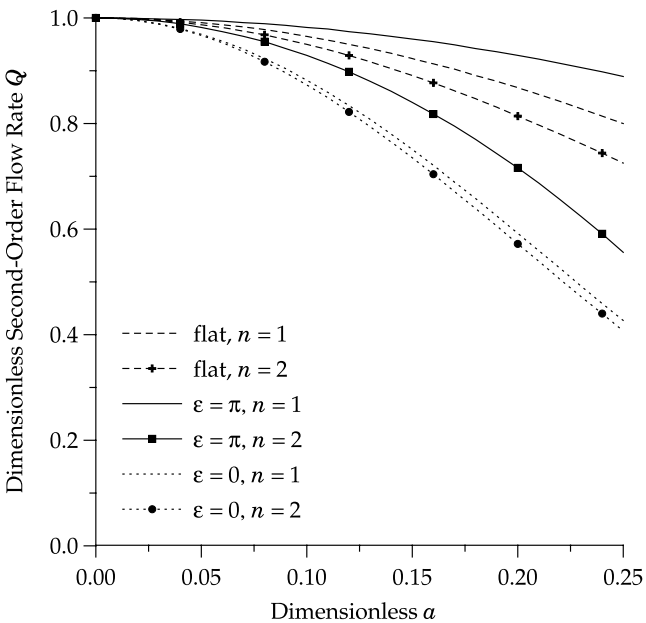

Figure 4. Second-order flow rate for various sinusoidal fracture wall configurations: one-cycle and two-cycle (symbols) mated ($\varepsilon = \pi$) (solid lines) and unmated ($\varepsilon = 0$) sinusoidal walls (dotted lines), and with a flat bottom (dashed lines). The perturbation parameter is $\delta = 0.3$ and the Reynolds number is zero.

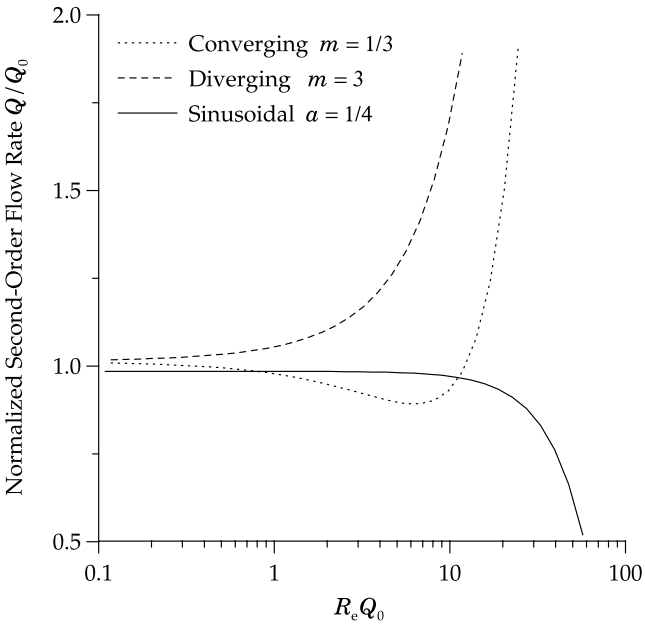

Figure 5. Normalized second-order flow rate in a converging, diverging, and sinusoidal fracture as a function of the Reynolds number. The perturbation parameter is $\delta = 0.3$.

the viscous dissipation effect is smaller for a fracture with one smooth wall since there is less disruption of streamlines.

[47] One can compare the results shown in Figures 2 and 4 with the lattice gas automata (LGA) simulations of *Brown et al.* [1995] for sinusoidal walls with either a steep slope ($a\delta = \sqrt{3}/8$) or a gentle slope ($a\delta = \sqrt{3}/32$) of the roughness. The trends shown in Figures 2 and 4 agree with the results shown in their Figures 3 and 4. For an amplitude of the roughness a of the same order as the separation gap of the maximum protrusions, which corresponds to $a = 0.25$ for symmetrical walls, the flow rate increases as the phase alignment increases from 0 to π. Using the Reynolds approximation, the relative magnitude of the increase varies from 1 to a maximum of $Q_0(\pi)/Q_0(0) = 1/0.43 = 2.3$; however, using the second-order estimate, the maximum variation between the different misalignments ε decreases, as shown in Figure 4. The Reynolds estimate for a perfectly aligned sinusoidal roughness ($\varepsilon = \pi$) is equal to 1 since the apparent aperture is constant everywhere in the fracture. The zero-order solution (Reynolds approximation) for mirror walls ($\varepsilon = 0$) gives $Q_0 = 0.43$, which is a factor of 2 lower than the parallel plate approximation. However, the second-order flow rate for a gently sloping roughness ($a = 0.25$ and $\delta = \sqrt{3}/8$) is equal to $Q = 0.42$, which is very close to the Reynolds estimate, while the second-order flow rate for a steeply sloping roughness ($a = 0.25$ and $\delta = \sqrt{3}/2$) is 10% lower and equal to $Q = 0.38$.

5.4. Effect of Inertia

[48] Figure 5 presents the second-order flow rate normalized with respect to the zero-order flow rate Q_2/Q_0 for $\delta = 0.3$ and for various flow conditions R_e^* whereby the Reynolds number is defined by $R_e^* = R_e Q_0$. Three different fracture geometries are considered: converging ($m = 1/3$) and diverging ($m = 3$) symmetrical linear walls, and symmetrical sinusoidal walls ($a = 0.25$). Equations (47) and (57) were used to plot the three curves. The three geometries are somewhat similar in that $\beta = b_{max}/b_{min} = 3$ in all three cases. It should also be mentioned that the effect of the vertical viscous dissipation is limited for these particular geometries. The Reynolds and the Stokes approximations of the flow rate are very close. Hence the effect of inertia through the presence of the Reynolds number is isolated from the effect of geometry and the viscous dissipation effects. Figure 5 shows that the contribution of the inertia term is dependent on the geometry of the fracture. The waviness of the sinusoidal fracture wall decreases the flow rate through viscous and inertia forces. The flow rate decreases due to the increase of viscous dissipation near the throats of the sinusoidal openings. The deviation of the flow rate from the Reynolds approximation is in agreement with the experimental results of *Iwai* [1976] reproduced by *Zimmerman and Yeo* [2000] and the LGA simulations of *Brown et al.* [1995]. The LGA simulation results pertain to the same geometry of a sinusoidal fracture with $a \approx 0.25$ and $\delta = \sqrt{3}/2$. The reduction of the flow rate shown in their Figure 5 is in very close agreement with the flow rate shown in Figure 5 for $R_e^* < 40$, noting, however, that the definition of their Reynolds number is equivalent roughly to $R_e^*/2$.

[49] For the diverging wall case $m > 1$, the flow rate increases monotonically for $R_e > 0$, while for the converging wall case, $m < 1$, the flow rate decreases with R_e^* before increasing again. In the latter case, the converging flow lines cause energy dissipation as the Reynolds number increase until the inertia effects overwhelm the viscous effects for higher Reynolds number. In the diverging fracture, the inertial effects accelerate the flow without causing much dissipation. This nonmonotonic behavior of the converging fracture can also be inferred from equation (57), where the factor $(m - 1)$ is positive for diverging fractures and negative for converging fractures. Hence the viscous and inertia terms are of opposite signs in converging fractures, which produces this nonmonotonic behavior. One should also note that the accuracy of the second-order perturbation solution might be breaking down at high Reynolds numbers and that higher-order terms might need to be included.

[50] The corresponding curve for a flat bottom wall is roughly the same (slightly lower) as for the mirror case if the ratio $b_{max}/b_{min} = 3$ is preserved. An increase in the value of δ creates also a similar trend as shown in Figure 5 but with a further deviation of the flow rate from 1 in the Stokes limit ($R_e^* = 0$). One can safely assume that the inertia effects can be neglected for $\delta R_e^* < 7$ for sinusoidal fractures and for $\delta R_e^* < 1$ for saw-toothed profiles for a tolerance level of 10% on the flow rate.

5.5. Effect of Seepage

[51] Figure 6 presents the entrance and exit flow rate as a function of the matrix conductivity parameter λ. The curves pertain to the second-order flow rate with $\delta = 0.3$ in a leaky parallel wall fracture $m = 1$ for various flow conditions, $R_e = 0$ and $R_e = 15$, and to the zero-order Stokes flow $R_e = 0$ in fractures of various top wall inclinations, $m = [1/3, 1/2, 3]$. The effect of inertia on the leaky fracture flow was limited to parallel walls because of the complexity of the resulting mathematical solutions for the case of linear walls. The results pertain also to the condition that the hydraulic head across the matrix is equal to the exit head value, $h_b = h_r$ i.e.,

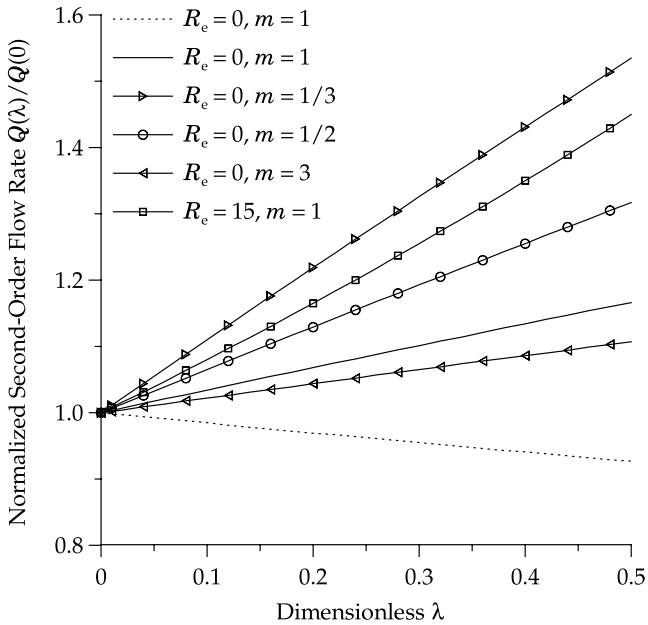

Figure 6. Second-order flow rate at entrance (solid) and exit (dotted) as a function of the matrix conductivity parameter for various wall inclinations and flow conditions. The flow rate is normalized with respect to the flow for impermeable wall conditions. The perturbation parameter is $\delta = 0.3$.

$H_b = 0$. The flow rates are normalized with respect to the zero-order flow rate for impermeable walls (equation (56)). Therefore a value different from 1 quantifies the error in assuming impermeable walls. For $\lambda = 0$, the entrance and exit flows are equal to 1, as expected. For increasing values of λ, the leakage into the matrix increases and the normalized flow rate deviates from 1. For $R_e = 0$ and $m = 1$, the entrance flow increases from 1 by more than 10% and the exit flow decreases from 1 since part of the entrance flow is lost to leakage. The deviation from 1 increases further for converging fractures ($m < 1$) while it is insensitive to the slope of the wall for diverging fractures ($m > 1$). For diverging walls, the entrance flow rate and the entrance to leakage flow rate ratio are independent of m and of the Reynolds number. The amount of total leakage increases from less than 5% of the entrance flow for a value of $\lambda = 0.1$ to 20% for $\lambda = 0.5$. For converging walls, the inclination of the top wall has a significant effect on the flow rate and the leakage rate because of the increase of the head within the converging fracture that provides a further driving force for seepage into the matrix. The exit flow rate is the same for a given slope m regardless if the fracture has a converging or a diverging top wall. It is close to and slightly lower than the exit flow rate for $m = 1$. The effect of inertia is to increase the flow rate at the entrance and at the exit in equal proportions as the leakage is almost independent of R_e for parallel walls.

5.6. Head Distribution

[52] Figure 7 presents the plot of the zero-order head distribution for impermeable and leaky parallel walls ($\lambda = 0.5$), impermeable linear ($\beta = 3$), and sinusoidal symmetrical ($a = 0.25$) fractures. The head distribution is obtained from equation (23) for impermeable walls and from equation (63) for the leaky wall case. For a linear variation of the fracture walls, the zero-order head distribution is not linear anymore. The head loss per unit length varies significantly from entrance to exit, while it is constant for a parallel fracture. The head profile for converging and diverging profiles shows a substantial head loss per unit length at the throat of the fracture. The throat is located at the entrance ($X = 0$) for the diverging fracture ($m > 1$) and at the exit ($X = 1$) for a converging fracture. The head distribution of a symmetrical sinusoidal fracture is sinusoidal revolving around the parallel wall head profile. The head distribution for a parallel impermeable fracture is linear and deviates from linearity for increasing values of leakage. However, the effect of leakage on the head distribution is relatively small. The effect of leakage for any geometric configuration is to decrease the head slightly, since seepage implies a head loss. The decrease in head is slightly greater for converging fractures than for diverging fractures because of the corresponding increase in seepage.

5.7. Velocity Profiles

[53] Figure 8 shows the velocity profiles for impermeable and leaky ($\lambda = 0.5$) parallel fracture, and impermeable symmetrical linear ($m = 3$) and sinusoidal ($a = 0.25$) fractures. The profiles are computed from the perturbation solution for the various geometries assuming $R_e = 20$ in order to accentuate the difference. The curves shown correspond to the velocity distribution at the entrance and at the exit of the fracture and at the maximum width for the sinusoidal fracture. The velocity profile is symmetric with respect to the centerline for impermeable fractures and skews downward for increasing leakage. The effect of inertia is to increase the maximum velocity variation from entrance to exit. Similarly, an increase in the wall inclination results in an increase of the difference between the profile at

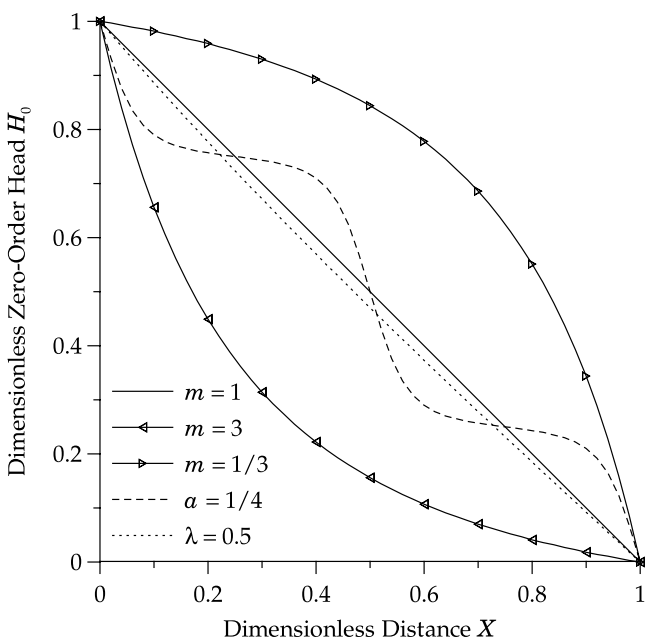

Figure 7. Zero-order head distribution for various flow and geometric configurations: leaky ($\lambda = 0.5$) and impermeable parallel fracture, symmetrical sinusoidal fracture, converging and diverging linear fracture.

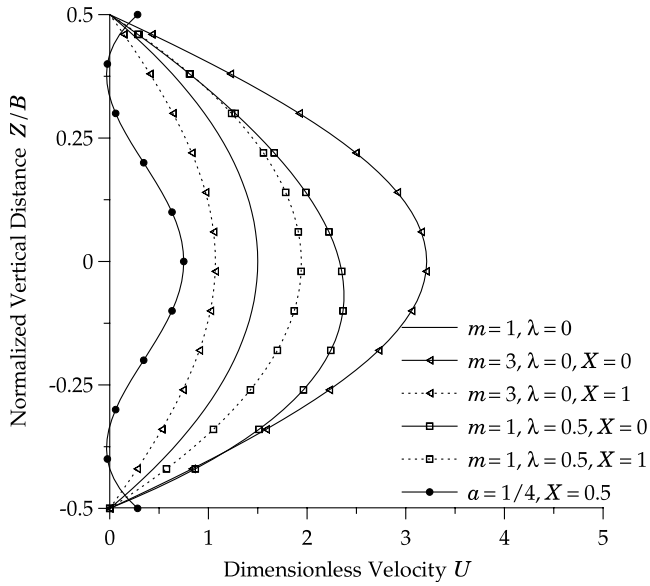

Figure 8. Second-order longitudinal velocity for parallel, linear ($m = 3$) and sinusoidal ($a = 0.25$) fracture geometry at entrance (solid) and exit (dotted). The leakage coefficient is $\lambda = 0.5$, the perturbation parameter is $\delta = 0.3$, and the Reynolds number is $R_e = 20$.

entrance and at exit. The maximum velocity for the diverging fracture ($m = 3$) varies from two thirds to twice the maximum velocity of a parallel plate. The velocity profile for a converging fracture is similar except that the maximum velocity occurs at the exit (throat) rather than at the entrance. The maximum velocity at both ends of a leaky parallel fracture is greater than their impermeable equivalent because of the increase in the flow rate for the same head gradient.

[54] Figure 8 shows that the velocity profiles are not parabolic for nonuniform apertures and leakage through the fracture walls, which clearly demonstrates the inapplicability of the Poiseuille flow assumption. Furthermore, the velocity profile at the wall cavity ($X = 0.5$) of the sinusoidal fracture shows a flow reversal in the wall cavity. There is a significant flow concentrated within a strip connecting the fracture throats and backflows near the walls. Flow separation is found to depend on the wall profile, its slope, and its curvature as well as on the Reynolds number. The primary cause of separation is the adverse pressure gradient, i.e., wherever the pressure increases in the downstream direction. The point of separation is that point on the boundary where the shear and the normal-gradient of the velocity are zero, i.e., when $\partial V_t/\partial n = 0$ at $Z = B_t$ where V_t is the tangential velocity. For sinusoidal profiles, the flow separates in the diverging region of the fracture for large roughness values of a, roughness frequency δ, and Reynolds number. However for linear profiles, there is no flow separation up to the second order. The second-order solution cannot capture the flow reversal developed in Jeffery-Hamel flows probably because the prescribed uniform head boundary conditions and the uniform wall profile preclude any flow reversal. The solution of the classical Jeffery-Hamel problem predicts a flow reversal for diverging nozzles at high Reynolds number, due to the presence of a source at the origin that creates a singular flow condition and a nonuniform head distribution at the boundaries.

[55] Nonetheless, the velocity profiles of the Jeffery-Hamel problem and the present one are close for $R_e = 0$. The Jeffery-Hamel flow problem assumes that the component velocities are of prescribed forms. The symmetrical radial velocity component is $V_r(r, \theta) = F(\theta)/r$ and the circumferential velocity is $V_\theta = 0$. These assumptions reduce the Navier-Stokes equations in polar coordinates for $R_e = 0$ to

$$F''' + 4\alpha^2 F' = 0 \quad F(-1) = 0 \quad F(0) = 1 \quad F(+1) = 0 \qquad (66)$$

where $F(\theta/\alpha) = V_r/V_{\max}$ is the normalized radial velocity profile with respect to the maximum velocity $V_{\max} = F(0)/r$ at the center axis of the fracture and α is the opening half angle. The variable r varies from a minimum of $(\csc\alpha - \sec\alpha)/2$ at the entrance to a maximum of $(\csc\alpha + \sec\alpha)/2$ at the exit of a diverging fracture. The radial velocity profile can be obtained from equation (66) using the definition of the total flow rate Q in polar coordinates. It is expressed as

$$V_{rJ} = \frac{Q}{r}\,\frac{\cos(2\theta) - \cos(2\alpha)}{\sin(2\alpha) - 2\alpha\cos(2\alpha)} \qquad (67)$$

Using the perturbation solution, the transformation of the velocity vector from the Cartesian coordinate to the radial coordinate with origin at the apex of the extended fracture walls shows that the circumferential velocity is zero and the velocity is only radial. In polar coordinates (r, θ), where $X = r\cos\theta - 1/(m-1)$ and $Z = [X + 1/(m-1)]\tan\theta$, the zero-order velocity components are given by $V_{r0} = +U_0\cos\theta + W_0\sin\theta$ and $V_{\theta 0} = -U_0\sin\theta + W_0\cos\theta$. Substituting the zero-order velocities, one obtains that $V_{\theta 0} = 0$ and

$$V_{r0} = \frac{3Q}{8r}\,\frac{\cos(2\theta) - \cos(2\alpha)}{\cos^4\theta}\,\frac{\cos\alpha}{\sin^3\alpha} \qquad (68)$$

A similar derivation using the second-order velocity terms would again show that $V_{\theta 2} = 0$ and provide a higher-order term to equation (68). A plot of equations (67) and (68) shows that the velocity profiles are quite close. The maximum difference is at the centerline $\theta = 0$ where the ratio V_{r0}/V_{rJ} is given by $(3/4)(\alpha + \cot\alpha - \alpha\cot^2\alpha)\cot\alpha$ and is roughly 0.90 for $\alpha = 0.5$.

5.8. Region of Validity

[56] The basic premise of the perturbation expansion is that the ratio of the vertical velocity over the longitudinal velocity is of the order of δ, as can be deduced from the definition of the dimensionless velocities (equation (7)). Hence the perturbation solution is valid so long as the dominant flow is in the longitudinal direction. The perturbation expansion is not well suited for fracture flows in which the dominant flow is bidirectional. For example, it is less valid for aligned or mated sinusoidal fracture walls ($\varepsilon = \pi$) than for sinusoidal fracture walls with mirror image roughness ($\varepsilon = 0$), especially for large amplitude or frequency of the corrugations since the flow path tends to follow the wall variation and the component velocities become of equal order $w/u = O(1)$.

[57] The present perturbation results compare well with the results of previous asymptotic studies. *Hasegawa and*

Izuchi [1983] derived the perturbation solution of the sinusoidal channel with a flat wall using the stream function formulation with similar boundary conditions and the same perturbation parameter δ. The two asymptotic solutions yield exactly the same results. The stream functions can be obtained from the above perturbation results by integrating the velocity expressions over the depth *Z*. Equations (21)–(25) of *Hasegawa and Izuchi* [1983] can be rederived by integrating the expressions for U_0, U_1, and U_2 over *Z*. Conversely, the flow rate can be obtained from the stream function results of *Hasegawa and Izuchi* [1983] by substituting $Z = B$ in their results. The flow rate for a sinusoidal fracture with a flat bottom wall (equation (49)) agrees with their equation (equations (29) and (30)) that was also referenced by *Zimmerman and Yeo* [2000, equation 16].

[58] *Kitanidis and Dykaar* [1997] presented a fourth-order perturbation solution of the Stokes equation for the symmetrical sinusoidal fracture using the same perturbation parameter δ but with a different auxiliary condition based on an energy argument. The second-order flow rate expression is given in integral form by their equations (33) and (34), which upon integration yields a result similar to equation (47) for $R_e = 0$ except for an extra numerical factor of 6 in the second-order term that is the result of the different boundary conditions. *Sisavath et al.* [2003] used the perturbation result of *Van Dyke* [1987] and the creeping flow assumption to obtain the second-order flow rate for the same sinusoidal geometry but with a different auxiliary condition and a different perturbation parameter. Their perturbation parameter was the roughness amplitude to wavelength ratio, and their second-order flow rate is given in a rational form.

[59] *Hasegawa and Izuchi* [1983] and *Sisavath et al.* [2003] assessed the extent of the error of their perturbation expansion by comparing with numerical models. *Hasegawa and Izuchi* [1983] showed that the flow rate results are accurate to within 10% for $\delta = 0.4$ and small R_e, and for $\delta = 0.3$ and $R_e \leq 50$. They also mentioned that the perturbation solution is more accurate for flow in symmetrical sinusoidal fractures. The latter statement was also corroborated by *Sisavath et al.* [2003], who found very good agreement between the perturbation and the numerical solution for the case of a symmetrical sinusoidal fracture for $\delta < 1$ and $a < 0.3$. Using Figure 3 of *Sisavath et al.* [2003], one can quantify the difference between the various perturbation solutions and their numerical model that uses a prescribed parabolic velocity distribution at the boundary. For $a = 0.3$ and $\delta = 0.5$, Figure 3 shows the numerical model result as $Q = 0.23$, the *Sisavath et al.* [2003] prediction gives $Q = 0.215$, the *Kitanidis and Dykaar* [1997] expression yields $Q = 0.197$, while equation (47) gives $Q = 0.264$. The difference in the various results is due to the approximation error involved as well as the different boundary conditions used in the various models. *Kitanidis and Dykaar* [1997] and *Sisavath et al.* [2003] specify the flow or velocity at the entrance of the fracture, while *Hasegawa and Izuchi* [1983] and the present work specify the pressure at the boundary.

[60] Figure 9 delineates the region in the $\delta - R_e$ parameter space for which the second-order flow rate and the zero-order flow rate (Reynolds approximation) differ by more than 10%. The region below the lines is the parameter space for which the Reynolds approximation holds and the inclusion of higher-order terms are not warranted. The curves correspond to contours of Q_2/Q_0 equal to 0.9 or 1.1. They pertain to a converging ($m = 1/3$) and a diverging ($m = 3$) symmetrical fracture, sinusoidal symmetric ($\varepsilon = 0$) and asymmetric fracture ($\varepsilon = \pi/2$) for $\beta = 2$ and $\beta = 3$ where $\beta = b_{max}/b_{min}$. The curves for linear fractures with different widths ratios *m* are close or within the two curves shown in Figure 9. The shapes of the curves corresponding to the diverging and converging fracture imply that the contribution of the higher-order terms is small for small Reynolds number and is significant at high Reynolds number even for small values of δ. Hence the zero-order solution by itself is insufficient to estimate the flow for high R_e^* even if δ is small. The contribution of the inertia terms is more significant for diverging than converging fractures.

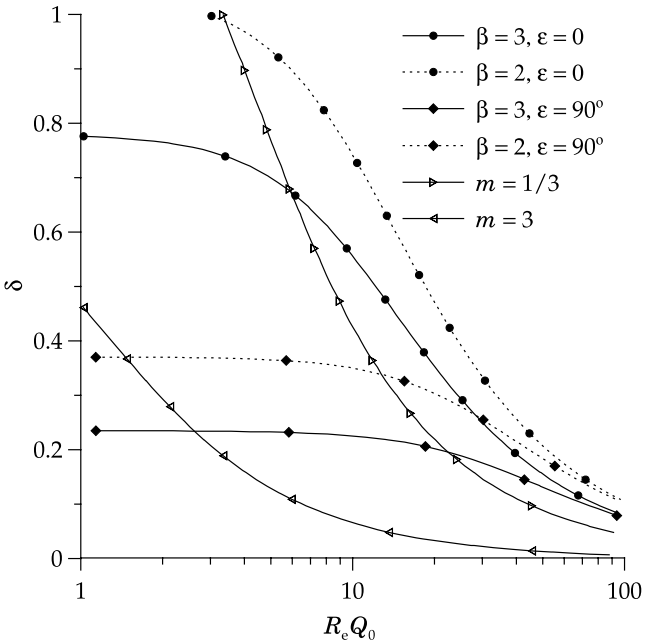

Figure 9. Region of the parameter space $\delta - R_e^*$ below which the second-order term is less than 10% of the zero-order term.

[61] For sinusoidal fractures, the location of the delineating curves is a function of the alignment of the corrugations and $\beta = b_{max}/b_{min}$. The sinusoidal symmetrical fracture curve follow the same trend as the linear fracture case in that the zero-order term is the dominant term for a wide range of δ and small R_e^* since the curves point upward for R_e^* near zero. As β increases, the curves shift downward, implying that the contribution of the higher-order terms becomes more significant for lower values of R_e^* and δ. Figure 9 clearly shows that the Reynolds approximation is valid for a wider range of R_e^* and δ for the symmetric fracture than for the asymmetric fracture. The contribution of the higher-order terms at $R_e^* = 0$ for the asymmetric fracture ($\varepsilon = \pi/2$) becomes important at $\delta = 0.37$ for $\beta = 2$ and at $\delta = 0.23$ for $\beta = 3$ and at smaller values of δ for increasing R_e^*. One can also use the solution of the mated sinusoidal walls ($\varepsilon = \pi$) to define the criterion for which the Reynolds equation applies. For the difference between the Reynolds approximation and the Stokes approximation to be within 10%, the second-order version of equation (46)

gives us that $\delta \leq (a\pi\sqrt{20})^{-1}$. For $a = 0.25$, the limit is roughly $\delta \leq 0.3$. The value of the perturbation parameter δ is also limited by the ratio of the vertical and longitudinal velocities. Numerical results show that this criterion is satisfied for misaligned sinusoidal variations ($\varepsilon = \pi/2$) if $\delta \leq a\ \pi/2$ and for mirror sinusoidal walls if $\delta \leq a\pi$.

6. Concluding Remarks

[62] We derived the perturbation solution of the two-dimensional Navier-Stokes equation for flow in fractures of simple geometries taking into account the effect of leakage into the adjoining soil matrix. The perturbation analysis provides the Reynolds lubrication approximation as the leading-order approximation and higher-order terms that incorporate the contribution of the roughness amplitude and frequency and the inertia effects. Flow rate expressions for various simple geometries were obtained as a function of the various parameters. Numerical results indicated the significant effect of the roughness and inertia on the estimation of the flow in fractures. The flow rate decreases significantly from its cubic law estimate for sinusoidal fractures, and only in instances of high inertia in diagonal fracture walls is the flow greater than the cubic law estimate. The contribution of the higher-order terms for creeping flow is insignificant for diagonal walls and symmetrical sinusoidal walls. Flow rate values for leaky fractures are significantly different from the flow rate estimate for impermeable walls condition. The numerical results also show that the head and velocity distribution deviate significantly from their respective linear and parabolic distribution of a parallel fracture. The flow rate expressions derived for the various simple geometries can constitute a basis for the formulation of conceptual models for numerical modeling of flow in discrete fracture networks and in fractured soils wherein there is a significant interaction between the fracture and the enclosing soil matrix. The derivative results of velocity profiles and flow reversal are also useful for studies that deal with transport processes in fractures. The above approximate solutions might provide a reliable tool for flow and transport predictions in fractured domain.

[63] **Acknowledgments.** This work was partially completed at Imperial College (IC), London, while the senior author was on faculty development leave from the American University of Beirut (AUB). The hospitality of the host institution IC and the support of the University Research Board at AUB are gratefully acknowledged. This work benefited significantly from discussions with R. W. Zimmerman at IC, who also provided some of the key references. Acknowledgment is also due M. Darwish at AUB for his assistance in the numerical simulation of the Navier-Stokes equation.

References

Brown, S. R., Fluid flow through rock joints: The effect of surface roughness, *J. Geophys. Res.*, *92*, 1337–1347, 1987.

Brown, S. R., H. W. Stockman, and S. J. Reeves, Applicability of the Reynold's equation for modeling fluid flow between rough surfaces, *Geophys. Res. Lett.*, *22*(18), 2537–2540, 1995.

Ge, S., A governing equation for fluid flow in rough fractures, *Water Resour. Res.*, *33*(1), 56–61, 1997.

Hasegawa, E., and H. Izuchi, On steady flow through a channel consisting of an uneven wall and a plane wall, 1, Case of no relative motion in two walls, *Bull. Jpn. Soc. Mech. Eng.*, *26*, 514–520, 1983.

Hildebrand, F. B., *Advanced Calculus for Applications*, 2nd ed., Prentice-Hall, Upper Saddle River, N. J., 1976.

Iwai, K., *Fundamental Study of Fluid Flow through a Single Fracture*, Ph.D. dissertation, Univ. of Calif., Berkeley, 1976.

Kitanidis, P. K., and B. B. Dykaar, Stokes flow in a slowly varying two-dimensional periodic pore, *Transp. Porous Media*, *26*, 89–98, 1997.

Oron, A. P., and B. Berkowitz, Flow in rock fractures: The local cubic law assumption reexamined, *Water Resour. Res.*, *34*(11), 2811–2825, 1998.

Pyrak-Nolte, L. J., L. R. Meyer, N. G. W. Cook, and P. A. Witherspoon, Hydraulic and mechanical properties of natural fractures in low permeability rock, in *Proceedings of the 6th International Congress on Rock Mechanics*, edited by G. Herget and S. Vongpaisal, pp. 225–231, A. A. Balkema, Brookfield, Vt., 1987.

Raven, K. G., K. S. Novakowski, and P. A. Lapcevic, Interpretation of field tracer tests of a single fracture using a transient solute storage model, *Water Resour. Res.*, *24*, 2019–2032, 1988.

Schlichting, H., and K. Gersten, *Boundary Layer Theory*, Springer-Verlag, New York, 2000.

Sisavath, S., A. Al-Yaarubi, C. C. Pain, and R. W. Zimmerman, A simple model for deviations from the cubic law for a fracture undergoing dilatation or closure, *Pure Appl. Geophys.*, *160*, 1009–1022, 2003.

Tsang, Y. W., and C. F. Tsang, Channel model flow through fractured media, *Water Resour. Res.*, *23*(3), 467–479, 1987.

Van Dyke, M., Slow variations in continuum mechanics, *Adv. Appl. Mech.*, *25*, 1–43, 1987.

Waite, M. E., S. Ge, and H. Spetzler, The effect of surface geometry on fracture permeability: A case study using a sinusoidal fracture, *Geophys. Res. Lett.*, *25*(6), 813–816, 1998.

Witherspoon, P. A., J. S. Y. Wang, K. Iwai, and J. E. Gale, Validity of cubic law for fluid flow in a deformable rock fracture, *Water Resour. Res.*, *16*, 1016–1024, 1980.

Zimmerman, R. W., and I. W. Yeo, Fluid flow in rock fractures: From the Navier-Stokes equations to the cubic law, in *Dynamics of Fluids in Fractured Rock*, *Geophys. Monogr. Ser.*, vol. 122, edited by B. Faybishenko, P. A. Witherspoon, and S. M. Benson, pp. 213–224, AGU, Washington, D. C., 2000.

H. A. Basha, Faculty of Engineering and Architecture, American University of Beirut, Beirut, Lebanon. (habib@aub.edu.lb)

W. El-Asmar, Department of Naval Architecture and Marine Engineering, University of Michigan, Ann Arbor, MI 48109, USA.